
aiMotive Dataset: A Multimodal Dataset for Robust Autonomous Driving with Long-Range Perception

Tamás Matuszka, Iván Barton, Ádám Butykai, Péter Hajas, Dávid Kiss
Domonkos Kovács, Sándor Kunsági-Máté, Péter Lengyel, Gábor Németh
Levente Pető, Dezső Ribli, Dávid Szeghy, Szabolcs Vajna, Bálint Varga

aiMotive

Budapest, Hungary

<https://aimotive.com>

Abstract

Autonomous driving is a popular research area within the computer vision research community. Since autonomous vehicles are highly safety-critical, ensuring robustness is essential for real-world deployment. While several public multimodal datasets are accessible, they mainly comprise two sensor modalities (camera, LiDAR) which are not well-suited for adverse weather. In addition, they lack far-range annotations, making it harder to train neural networks that are the base of a highway assistant function of an autonomous vehicle. Therefore, we introduce a multimodal dataset for robust autonomous driving with long-range perception. The dataset includes 176 scenes with synchronized and calibrated LiDAR, camera, and radar sensors covering a 360-degree field of view. The collected data was captured in highway, urban, and suburban areas during daytime, night, and rain and is annotated with 3D bounding boxes with consistent identifiers across frames. Furthermore, we trained unimodal and multimodal baseline models for 3D object detection. Data and code are available at https://github.com/aimotive/aimotive_dataset.

1 Introduction

A large number of datasets for 3D object detection applied in autonomous driving have been released in the last few years (Geiger et al., 2012b; Chang et al., 2019; Huang et al., 2018; Pham et al., 2020; Patil et al., 2019; Caesar et al., 2020). Most datasets have the common property of including sensor data from different modalities, such as cameras and LiDAR. In this way, a 360-degree field-of-view (FOV) can be covered around the ego vehicle. 3D object detection datasets can be split into groups based on the coverage around the ego vehicle and sensor redundancy. While numerous datasets are publicly available, they either do not provide sensor redundancy (i.e. sensor coverage by at least two sensor modalities) which is essential for robust autonomous driving or rely only on camera and LiDAR sensors that are not perfectly applicable in adverse weather (see Table 1 for the properties of several popular datasets grouped based on sensor coverage and redundancy). This issue can be solved by utilizing radars that is a cost-effective sensor and is not affected by adverse environmental conditions (e.g. rain or fog). Furthermore, the annotation range does not exceed 80 meters (with a few exceptions), which is insufficient for training long-range perception systems. The limitation of the annotation range can be explained by the fact that autonomous driving datasets mainly focus on urban environments while ensuring the ability to detect objects in distant regions is critical for highway assistants and therefore for autonomous driving.

Dataset	Ours	nuScenes	Lyft	Argo2	Waymo	ONCE	Radiate	RADial	DENSE
Ann. Scenes	176	1000	366	1000	1150	581	61	91	N/A
Ann. LiDAR frames	26.5k	40k	46k	150k	230k	16k	44k	8.3k	13.5k
3D boxes	427k	1.4M	1.3M	11.25M	12M	412k	203k	9.5k	100k
Classes	14	23	9	30	4	5	8	1	4
Camera	4	6	7	9	5	7	2	1	2
Radar	2	5	-	-	-	-	1	1	2
LiDAR	1	1	3	2	5	1	1	1	1
Range	< 200m	<100m	<100m	< 200m	<100m	<100m	<100m	<100m	<100m
Countries	3	2	1	1	1	1	1	1	4
Continents	2	2	1	1	1	1	1	1	1
Night	✓	✓	✗	✓	✓	✓	✓	✗	✓
Rain	✓	✓	✓	✓	✓	✓	✓	✗	✓
Highway	✓	✗	✗	✗	✗	✗	✓	✓	✓

Table 1: Comparison of relevant datasets. Middle group: datasets with redundant 360° sensor coverage, right group: datasets with 360° view without sensor redundancy. Range refers to the perception limit of the front and back region in the case of the middle group and the front area for the right group (ego vehicle is the origin).

Therefore, we release a multimodal dataset for robust autonomous driving with long-range perception to overcome the abovementioned limitations. The collected dataset includes 176 scenes with synchronized and calibrated LiDAR, camera, and radar sensors covering a 360-degree field of view. The data was captured in diverse geographical areas (highway, urban, and suburban) and different time and weather conditions (daytime, night, rain). We provide 3D bounding boxes with consistent identifiers across frames that enable the utilization of our dataset for 3D object detection and multiple object tracking and prediction tasks. The proposed dataset is published under CC BY-NC-SA 4.0 license, allowing the research community to use the gathered data for non-commercial research purposes. Our main contributions are the followings:

- We released a multimodal autonomous driving dataset with redundant sensor coverage (including radars) and 360° FOV.
- Our dataset has an extended annotation range compared to existing datasets allowing the development of long-range perception systems.
- We trained and benchmarked unimodal and multimodal baseline models.

By releasing our dataset and models to the public, we seek to facilitate research in multimodal sensor fusion and robust long-range perception systems.

2 Related work

One of the most influential datasets is KITTI by Geiger et al. (2012b), which generated interest in 3D object detection in autonomous driving. The KITTI dataset contains 22 scenes recorded in Karlsruhe, Germany. The sensor setup consists of front cameras and a roof-mounted LiDAR. The perception range of the released dataset is less than 100 meters, and no 360-degree FOV is provided. In addition, the footage was recorded only in the daytime.

Several popular 3D object detection datasets provide a 360° FOV with sensor redundancy. Among these, nuScenes (Caesar et al., 2020) is the most similar dataset to our work, including full sensor redundancy for the entire sensor setup. However, a 32-beam LiDAR with a relatively sparse point cloud and limited perception range was used during the recording process, resulting in a shorter perception limit than 100 meters (i.e. there are no annotated objects with a distance larger than 100 meters from the ego vehicle at the moment when the given frame was annotated). The sensor data has been recorded in urban environments (Boston, USA, Singapore) and lacks footage on highways. Waymo Open Dataset (Sun et al., 2020) is the first large-scale autonomous driving 3D object detection data collection with 360° FOV, including more than 1000 scenes and 12M annotated objects.

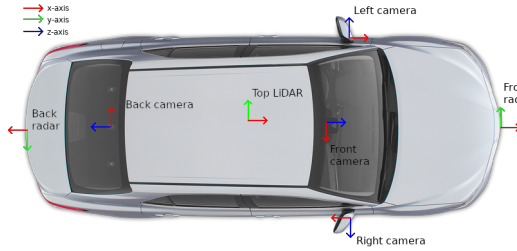


Figure 1: Sensor setup and coordinate systems.

Sensor	Details
1x LiDAR	Spinning, 64 beams, 10Hz capture frequency, 360° horizontal FOV, +15° to -25° vertical FOV, $\leq 200m$ range, ± 2 cm accuracy, up to 1.15 Million Points per Second
2x Radar	18 Hz capture frequency, 77GHz, -16° to +16° azimuth FOV, -7.5 to +7.5 elevation FOV, up to 175m distance, velocity accuracy of ± 0.1 m/s
4x Camera	2x fisheye: 30 to 60 Hz capture frequency, 1/2.7" CMOS sensor of 1920 \times 1080 resolution, 2x pinhole: 30 to 40 Hz capture frequency, 1/1.55" CMOS sensor of 2896 \times 1876 resolution
1x GNSS+INS	up to 100 Hz measurement frequency, position accuracy of 100 mm (PPK), heading accuracy of 0.044°, roll&pitch accuracy of 0.009°

Table 2: Description of used sensors.

The main shortcoming of this dataset is the limited perception range and sensor suite. The recently released Argoverse2 Sensor (Wilson et al., 2021) dataset utilized the experiences gained from hosting several challenges using the Argoverse (Chang et al., 2019) dataset. Argoverse2 has a similar scale as Waymo Open Dataset but with an extended annotation range. The disadvantage of the dataset compared with our solution is the lack of radar sensor usage and the diversity of recording locations (see Table 1). Both Lyft Level 5 perception dataset (Kesten et al., 2019) and ONCE (Mao et al., 2021) have recordings from only one country, without using any radars, and do not contain annotated objects in distant areas. Radiate (Sheeny et al., 2021) uses three different sensor modalities and contains a large amount of annotated keyframes in adverse weather (e.g. fog, rain, snow). The paper’s main contribution is the release of a high-resolution radar dataset. However, the perception range is limited (i.e. less than 100 m), and other sensor modalities are constrained (32-beam LiDAR with very sparse point cloud, only front camera with low-resolution images).

Another group of datasets also provides 360-degree coverage without ensuring sensor redundancy which is essential for robust autonomous driving. RADIAL(Rebut et al., 2022), similar to Radiate, employs a high-definition radar for sensing in 360°. The recorded data covers a wide range of geographical areas; however, the sensor setup is restricted to only three sensors. Furthermore, only a limited amount of annotated objects (less than 10k) are contained in the dataset. DENSE (Bijelic et al., 2020) also focuses on data collected in severe weather. The paper describes a unique sensor setup consisting of a thermal camera, gated cameras, and a spinning LiDAR. Even though a diverse set of sensors is mounted to the recording car, sensor redundancy is not ensured in the case of the dataset. Moreover, the annotated area is limited due to the challenging weather conditions.

Our dataset has an advantage over the existing related work, as is seen in Table 1. The proposed dataset combines sensor redundancy with a long perception range in diverse environments, which is not assured by previously published 3D object detection datasets. Ensuring these properties are required for training neural networks that can serve as a base for robust autonomous driving software operating in different environments.

3 aiMotive Multimodal Dataset

Our multimodal dataset comprises 15s long scenes with synchronized and calibrated sensors. The dataset provides a 360° FOV with the help of a redundant sensor layout. Thus, the surrounding area of the ego vehicle is recorded by at least two different sensors. Since the annotated 3D bounding boxes have consistent identifiers across frames within a scene, the dataset can be used for 3D object detection and multiple object tracking and prediction tasks. In addition, a considerable amount of annotations (about 25%) are located in the far-distance region ($\geq 75m$) concerning the ego vehicle. Due to this property and the redundant sensor setup, our dataset can facilitate research in multimodal sensor fusion and robust long-range perception systems.

	Highway	Urban	Night	Rain
All	45.8%	35.4%	15.0%	3.8%
Train	46.3%	34.4%	16.6%	2.7%
Val	43.4%	39.4%	8.6%	8.6%

	Length	Width	Height
Car	4.20	1.93	1.63
Pedestrian	0.77	0.75	1.77
Motorcycle	2.02	0.89	1.53
Bicycle	1.58	0.82	1.54

Table 3: Data distribution w.r.t weather and environment. Table 4: Average cuboid dimensions (m).

3.1 Data collection

The data was collected in three countries on two continents with four cars to provide a diverse dataset. The recordings have taken place in California, US; Austria; and Hungary using three Toyota Camry and one Toyota Prius. The recording phase of the footage was spread across a year to gather data in different seasons and weather conditions. As a result, our dataset consists of a diverse set of locations (highway, suburban, urban), times (daytime, night), and weather conditions (sun, cloud, rain, glare). The data collection method has satisfied the requirements given by the Institutional Review Board approval.

3.2 Sensor setup

Sensor layout. The data was recorded using a roof-mounted, rotating 64-beam LiDAR, four cameras, and two long-range radars, providing 360° coverage with sensor redundancy. The localization was based on a high-precision GNSS+INS sensor. Additional details can be found in Figure 1 and Table 2.

Synchronization. All of the recorded sensor data are synchronized. The LiDAR and radars share the same timestamp source. Our cameras capture images using the rolling shutter method, which scans the environment rapidly instead of capturing the image as a snapshot of the entire scene at a single time moment. Since the used cameras capture the scene row by row, the camera timestamp is approximately the exposure time when the middle row is captured.

Coordinate systems. The dataset uses five coordinate systems. Namely global, body, radar, camera, and image coordinate systems. We have used ECEF (Snay & Soler, 1999) as the global coordinate system and provided a 6-DOF ego-vehicle pose for each annotated frame. The reference coordinate system used for defining the annotated objects is called the body coordinate system and is assigned to the vehicle body. The origin is the projected ground plane point under the center of the vehicle’s rear axis at nominal vehicle body height and zero velocity. The radar coordinate system uses the same axes as the body coordinate system (x -axis positive forward, y -axis positive to the left, and z -axis positive upwards). The LiDAR point cloud was transformed into the body coordinate system as a preprocessing step. The origin of the camera coordinate system is the camera’s viewpoint, and the axes are defined the same as the OpenCV(Kaehler & Bradski, 2016) camera coordinate system (x -axis positive to the right, y -axis positive downwards, z -axis positive forward). Camera-to-body and radar-to-body transformations can be performed using camera and radar extrinsic matrices. We utilized OpenCV’s image coordinate system to render annotations using intrinsic matrices to project from camera coordinates to image coordinates.

3.3 Ground truth generation

We used two approaches for generating ground truth labels: an automatic annotation method for training data generation and manual annotation for creating validation data. The automatic annotation relies on LiDAR measurements and searches possible candidates in the entire point cloud of a 15s long sequence. Non-causal object tracking (i.e. both directions in time) including the association of new detections to the existing tracks is realized in the 2.5D descriptor space with the joint probability distribution of the modeled detection uncertainty and object dynamics. Utilizing the informative point cloud along with the

physical constraints, the consecutive detections (i.e. positions and orientations) of the same object can be optimized recursively. In this way, the point cloud of a given object can be accumulated from different views. As the tracked object’s trajectory becomes more accurate with the optimization steps, the model point cloud of the detected object becomes sharp; thus, a bounding box can be fitted on it. The annotated sequences were manually quality-checked based on multiple criteria. This inspection checks the position ($<10\%$ divergence between the object centroid and the cuboid centroid), orientation (within 5 degrees of precision), and size ($<10\%$ divergence between the object size and the cuboid size) of the amodal bounding boxes projected back to all available cameras. Since the sensors are mounted in different positions, some annotated objects may be occluded on specific sensors. The manual quality checking is performed on the scene level. Some label noise still might be in the dataset even though we aimed to minimize it via human validation. In this way, we selected sufficiently accurately labeled recordings, and most scenes with erroneous annotations were discarded.

In the case of the validation set, we hired manual annotators to label objects on the recorded sensor data. The human annotators used LiDAR and camera sensor data during the annotation phase to fit cuboids on any object of interest appearing on the camera images. For the cuboid sizes, annotators used default dimensions. If the default dimensions do not match the size of a given object in the point cloud or on the images, the annotators refined the non-matching dimensions of the given cuboid based on their own decision. The manual labor also ensured that the cuboid axes aligned with the object orientation within 5 degrees of precision.

The manually or automatically annotated objects belonging to 14 classes are represented as 3D cuboids with some additional physical properties. Each labeled bounding box has a 3D center point, 3D extent (length along the horizontal x -axis, width along the vertical y -axis, height along the z -axis), orientation (represented as a quaternion), relative velocity, and a unique track ID. Furthermore, we provide 2D bounding boxes utilizing a pretrained FCOS (Tian et al., 2019) detector. The 2D-3D annotations are associated using the Hungarian algorithm (Kuhn, 1955) for allowing the utilization of 2D-3D consistency or semi-pseudo-labeling (Matuszka & Kozma, 2022). The resulting dataset was anonymized using Dashcam-Cleaner¹.

3.4 Dataset analysis

The dataset includes 26 583 annotated frames with sensor data from multiple modalities, split into 21 402 train and 5 181 validation frames (151/25 train/val scenes). The scenes were recorded in diverse weather and environmental conditions. See Table 3 for the data distribution. Since the training and validation splits were generated with different methods, some distribution shifts between the data partitions might arise. We investigated the distribution of scenes concerning weather/environment and object count/dimensions and found that training and validation splits are similar in proportion.

The dataset contains more than 425k objects organized into 14 categories. See the class distribution in Figure 2. The distance distribution of the annotated objects is visualized in Figure 3. About 24% of the cuboids are beyond 75 m, Argoverse2 has about 14%, Waymo, nuScenes, and ONCE have less than 1%. This property enables the training of long-range perception systems with the help of our dataset.

Several additional statistics of the generated dataset are described by Table 4, Table 5, and Figure 4. The average cuboid dimensions for distinguished classes help to understand how precise the cuboids are per class. The number of average cuboids per environment indicates how crowded the scenes are. The percentage of empty boxes beyond 50 m and 75 m after the annotation process is 4.2% and 5.4%, respectively, as opposed to the conventional benchmarks where almost 50% of objects beyond 50 m contain zero LiDAR points (Gupta et al., 2023).

¹<https://github.com/tfahse/DashcamCleaner>

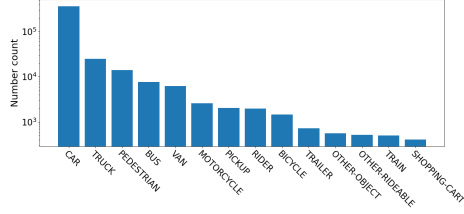


Figure 2: Class distribution.

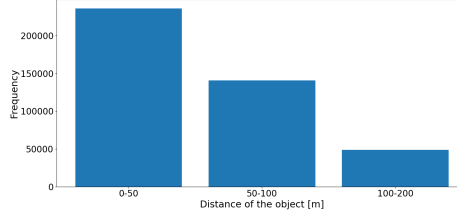


Figure 3: Distance distribution of annotated objects.

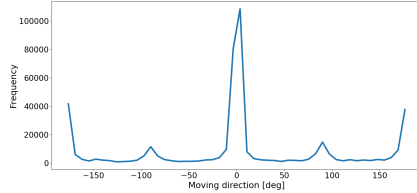


Figure 4: Orientation distribution of annotated objects.

(a) Mean density of scenes.		(b) Points in cuboids.	
	Cuboids/scene		
Urban	30	0-50 m	1209 2378
Highway	7	50-75 m	91 126
Night	14	75+ m	25 33
Rain	6		

Table 5: Additional statistics of the annotations.

4 Experiments

We trained several 3D object detection baselines on our dataset utilizing publicly available models. In order to exploit annotations located in distant areas, we defined the target grid as $[-204.8, 204.8]$ m in longitudinal and $[-25.6, 25.6]$ m in lateral directions. We mapped the 14 classes included in the dataset into four categories (car, truck/bus, motorcycle, pedestrian), then evaluated the model performance using the all-point and 11-point interpolated Average Precision (AP) metrics (Everingham et al., 2010) in Bird’s-Eye-View (BEV) space in a class agnostic manner. The Hungarian method (Kuhn, 1955) is used for associating ground truth and predictions with a 0.3 IoU threshold. We selected a small IoU value for the association threshold to handle displacement errors which are especially frequent in distant regions in BEV. Furthermore, the Average Orientation Similarity (AOS) (Geiger et al., 2012a) metric is utilized for evaluating the performance of the models in terms of orientation prediction.

4.1 Baseline models

Our baseline models are based on VoxelNet (Zhou & Tuzel, 2018), BEVDepth (Li et al., 2022), and BEVFusion (Liu et al., 2022) for LiDAR, camera, and multimodal models. Since BEVFusion does not use radar sensors, we designed a simple solution for LiDAR-radar fusion. Namely, we treated the radar point cloud as a regular LiDAR point cloud. After a point cloud merging step, data from different modalities can be processed by VoxelNet as if it was a regular LiDAR point cloud.

VoxelNet can operate on the point cloud directly and consists of three main parts. The Voxel Feature Encoder (VFE) is responsible for encoding raw point clouds at the individual voxel level. VoxelNet utilizes stacked VFE layers, and their output is further processed by a middle convolutional neural network (CNN) to aggregate voxel-wise features. The final component performing the 3D object detection is the region proposal network (Ren et al., 2015).

BEVDepth is a camera-only 3D object detection network that provides reliable depth estimation. The main observation of the authors is that recent camera-only 3D object detection solutions utilizing pixel-wise depth estimation generate suboptimal results due to inadequate depth estimation. Therefore, explicit depth supervision encoding intrinsic and extrinsic parameters is utilized. In addition, a depth correction subnetwork is introduced using sparse depth data from a LiDAR point cloud to provide supervision for the depth estimation network.

Modalities	Highway	Urban	Night	Rain	Full	Highway	Urban	Night	Rain	Full	AOS
LiDAR	0.755	0.608	0.746	0.477	0.663	0.731	0.600	0.727	0.480	0.649	0.594
LiDAR, camera	0.772	0.656	0.786	0.459	0.667	0.748	0.641	0.761	0.468	0.642	0.830
LiDAR, radar	0.769	0.617	0.732	0.454	0.668	0.745	0.607	0.748	0.465	0.658	0.509
LiDAR, radar, camera	0.762	0.644	0.730	0.423	0.658	0.740	0.630	0.708	0.435	0.652	0.851

Table 6: Comparison of baseline models. First group: all-point AP metric, second group: 11-point interpolation AP metric, third group: AOS metric averaged over val set.

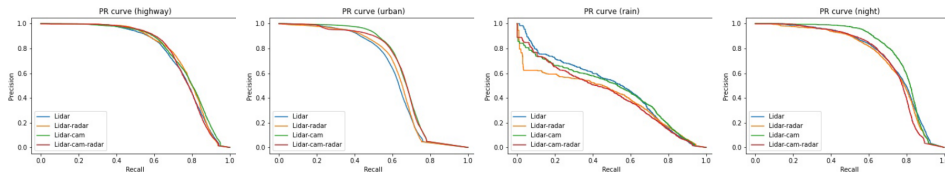


Figure 5: PR curves of baseline models.

The main contribution of BEVFusion is the utilization of the BEV space as the unified representation for camera and LiDAR sensor fusion. The image backbone proposed by BEVFusion explicitly predicts a discrete depth distribution for each image pixel, similar to BEVDepth (without the depth correction subnetwork). Then, a BEV pooling operator is applied on the 3D feature point cloud that is later flattened along the z -axis to get a feature map in BEV. The point cloud produced by a LiDAR is processed the same way as in the case of VoxelNet. Then, the two BEV feature maps are fused by a CNN. Finally, the detection heads are attached to the output of the fusion subnetwork.

4.2 Implementation details

The LiDAR components of the baseline models use HardSimpleVFE (Yan et al., 2018) as the Voxel Feature Encoder and SparseEncoder (Yan et al., 2018) as the middle encoder CNN. The image components adopt Lift-Splat-Shoot (Phillion & Fidler, 2020) as an image encoder with a ResNet-50 backbone followed by a Feature Pyramid Network (Lin et al., 2017) for leveraging multi-scale features. An additional depth correction network is also part of the image stream, inspired by BEVDepth. In the case of multimodal models, features from different modalities are fused using a simple fusion subnetwork consisting of convolution and Squeeze-and-Excitation (Hu et al., 2018) blocks. Finally, a CenterPoint (Yin et al., 2021) head is responsible for detecting objects from the BEV features, both in unimodal and multimodal cases.

Since our goal is not to develop state-of-the-art models in this work but to facilitate multi-modal object detection research, we used the hyperparameters provided by BEVDepth² without any heavy parameter tuning. We adapted the grid resolution to enable long-range detection, then trained the models for 16k iterations (3 epochs) using batch size 4 with a learning rate of $6.25e^{-5}$ using flip, rotation, and scale augmentations in the BEV feature space. We used an NVIDIA A100 TensorCore GPU for neural network training. The models are implemented using mmdetection3d³ and are publicly available on the dataset repository.

4.3 Experimental results

The performance comparison of the baseline models on different metrics is described in Table 6. Since the literature describes several examples (Qian et al., 2022; Liu et al., 2022) of the superiority of LiDAR-only unimodal solutions over camera-only models, we did not train a camera-only baseline. As the table describes, every multimodal model overperforms the LiDAR-only baseline in highway and urban environments in non-adverse weather and time. The additional sensor signals significantly increase detection performance in the dense urban environment. However, the unimodal baseline performs best in heavy rain, where

²<https://github.com/Megvii-BaseDetection/BEVDepth>

³<https://github.com/open-mmlab/mmdetection3d>

Modalities	Highway	Urban	Night	Rain	Full	Highway	Urban	Night	Rain	Full	AOS
LiDAR	0.526	0.470	0.464	0.617	0.473	0.521	0.472	0.477	0.612	0.466	0.858
LiDAR, camera	0.509	0.466	0.513	0.534	0.472	0.511	0.468	0.503	0.527	0.488	0.793
LiDAR, radar	0.522	0.525	0.550	0.652	0.478	0.522	0.519	0.546	0.644	0.484	0.868

Table 7: Comparison of baseline models in the distant region ($>75m$). First group: all-point AP metric, second group: 11-point interpolation AP metric, third group: AOS metric averaged over the validation set.

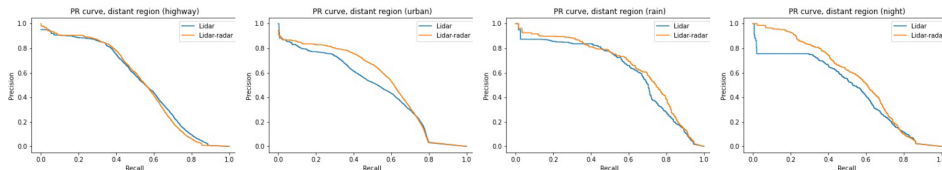


Figure 6: PR curves of baseline models in distant region ($>75m$).

one would think a radar signal should help to increase performance. This phenomenon suggests that more sophisticated radar fusion techniques might be beneficial for enhancing multimodal models.

Cameras play a crucial role in terms of orientation prediction. The models without RGB images struggle to consistently keep the orientation, especially in the case of large vehicles. This flickering effect is less visible for models using camera sensors. The model using all modalities performs best on the AOS metric.

Surprisingly, the model using LiDAR + camera modalities overperforms all other models in the night and urban environments by a large margin. We investigated the learning curves and found that increasing the number of training steps can help to enhance performance further. To validate our hypothesis, we trained our models for five additional epochs. Unfortunately, models using camera sensors became unstable after the third epoch and caused an explosion in the depth loss. Table 8 describes the result of the longer training process using the 11-point interpolation AP metric. A solid improvement can be seen in all environments, especially on the rainy validation set (+8.8/+5.2 AP for LiDAR and LiDAR+radar models, respectively). This can be explained by the fact that the detection heatmaps became sharper after more prolonged training. Blurry heatmaps were responsible for lower AP metrics in the case of the first group of baseline models. The blurring effect on the heatmap was distinctly visible around the ego car in heavy rain due to LiDAR reflections from raindrops.

In order to validate the long-range perception capabilities of the baseline models, we benchmarked the longer-trained models on distant object detection. Detections and ground truth were filtered out where the distance from the ego car was less than 75 meters. The results are summarized in Table 7. All models except LiDAR + camera perform similarly in the highway environment without any significant difference in performance. However, the model with additional radar signals significantly overperforms the LiDAR-only baseline in all other domains. The fact that radar sensors provide reliable and accurate signals for perceiving objects in distant areas, even in adverse weather, can be leveraged for boosting 3D object detector performance, as can be seen in Figure 6. A similar effect can be observed in a dense urban environment where radar signals are utilized by the multimodal baseline that resulted in a significant performance increase in long-range perception (+5.5/+4.7 all-point / 11-point interpolation AP). The overall performance on the whole dataset of the multimodal models is also better considering the 11-point interpolation metric.

The training results demonstrate that our dataset can serve as a base for multimodal long-range perception neural network training. Advanced evaluation techniques such as test-time augmentation or model ensembling could lead to further improvements. However, none of them were applied during the evaluation method. Table 8 suggests that further improvements in sensor fusion methods are needed for fully leveraging each modality, and our naive approach provides a suboptimal solution (especially in the case of heavy rain). Nevertheless,

Modalities	Highway	Urban	Night	Rain
LiDAR	0.757 (+2.6)	0.630 (+3.0)	0.754 (+2.7)	0.568 (+8.8)
LiDAR, radar	0.741 (-0.4)	0.638 (+3.1)	0.766 (+2.2)	0.517 (+5.2)

Table 8: Effects of longer training.

we hope the research community will find our dataset valuable and can build on our baselines, and will significantly improve its performance.

5 Additional proposed tasks

We propose additional tasks benefiting from our dataset besides 3D object detection. Since unique track IDs are provided, end-to-end long-range multiple object tracking models can also be trained with the help of the dataset. Multiple Object Tracking Accuracy (MOTA) and Multiple Object Tracking Precision (MOTP) metrics can be used for evaluating model performance.

Another proposed task is motion prediction. The ego-motion is included in the dataset and the trajectories of exo-objects can be computed using the unique track IDs. We propose a specific case of motion prediction, namely lead car prediction, which is essential for autonomous driving functions such as Automatic Emergency Braking or Adaptive Cruise Control. The lead cars can be determined by the intersection of ego-motion and the trajectories of exo-objects. The proposed task is to detect and predict the current and future lead vehicles. The model performance can be measured using precision and recall metrics.

The dataset also includes high-quality GNSS-INS sensory data, thus enabling the training and benchmarking of various odometry algorithms. Finally, the dataset can be used for contrastive representation learning. A similar representation can be learned for different sensor modalities corresponding to the same frame in a self-supervised manner which might be a valuable method for a model to acquire a consistent world representation from multiple sensors.

6 Conclusion

In this paper, we present a multimodal dataset for robust autonomous driving with long-range perception. Our diverse dataset recorded in three countries on two continents includes sensor data from LiDAR, radars, and cameras providing redundant 360-degree sensor coverage. The dataset contains a large number of annotated objects in distant areas, allowing the development of multimodal long-range perception neural networks. In addition, we developed several unimodal and multimodal baseline models and compared their performance on the proposed dataset based on different criteria. We showed that our dataset is suitable for training multimodal long-range perception neural networks leveraging the advantages of the recorded sensor modalities.

Limitations. The sensor setup results in a synchronization limitation caused by the fact that sensors differ in the temporal recording method. Since the rotating LiDAR and rolling shutter cameras have different measurement methods, there are some discrepancies in temporally discretized annotations. This phenomenon is mostly visible when the relative speed difference between the ego and exo car is large. Furthermore, though the entire FOV is covered by at least two sensor modalities, the dataset lacks side radars which would be beneficial for providing full sensor coverage. Fisheye cameras used on the sides give distorted images and shorter visibility range than pinhole cameras which might limit the performance for long-range detection in the side areas.

Future work. We aim to extend our collected dataset with additional environmental and weather conditions. Furthermore, we will conduct more in-depth experiments regarding sensor fusion for multimodal neural networks to overcome the detected weaknesses of the proposed fusion method. We seek to facilitate research in multimodal sensor fusion and robust long-range perception systems by releasing our dataset.



Figure 7: Example ground truth annotations from the training set (best viewed by zooming in).

References

- Mario Bijelic, Tobias Gruber, Fahim Mannan, Florian Kraus, Werner Ritter, Klaus Dietmayer, and Felix Heide. Seeing through fog without seeing fog: Deep multimodal sensor fusion in unseen adverse weather. In *Proceedings of the IEEE/CVF Conference on Computer Vision and Pattern Recognition*, pp. 11682–11692, 2020.
- Holger Caesar, Varun Bankiti, Alex H Lang, Sourabh Vora, Venice Erin Liong, Qiang Xu, Anush Krishnan, Yu Pan, Giancarlo Baldan, and Oscar Beijbom. nuscenes: A multimodal dataset for autonomous driving. In *Proceedings of the IEEE/CVF conference on computer vision and pattern recognition*, pp. 11621–11631, 2020.
- Ming-Fang Chang, John Lambert, Patsorn Sangkloy, Jagjeet Singh, Slawomir Bak, Andrew Hartnett, De Wang, Peter Carr, Simon Lucey, Deva Ramanan, et al. Argoverse: 3d tracking and forecasting with rich maps. In *Proceedings of the IEEE/CVF Conference on Computer Vision and Pattern Recognition*, pp. 8748–8757, 2019.
- Mark Everingham, Luc Van Gool, Christopher KI Williams, John Winn, and Andrew Zisserman. The pascal visual object classes (voc) challenge. *International journal of computer vision*, 88(2):303–338, 2010.
- Andreas Geiger, Philip Lenz, and Raquel Urtasun. Are we ready for autonomous driving? the kitti vision benchmark suite. In *2012 IEEE conference on computer vision and pattern recognition*, pp. 3354–3361. IEEE, 2012a.
- Andreas Geiger, Philip Lenz, and Raquel Urtasun. Are we ready for autonomous driving? the kitti vision benchmark suite. In *2012 IEEE conference on computer vision and pattern recognition*, pp. 3354–3361. IEEE, 2012b.
- Shubham Gupta, Jeet Kanjani, Mengtian Li, Francesco Ferroni, James Hays, Deva Ramanan, and Shu Kong. Far3det: Towards far-field 3d detection. In *Proceedings of the IEEE/CVF Winter Conference on Applications of Computer Vision*, pp. 692–701, 2023.
- Jie Hu, Li Shen, and Gang Sun. Squeeze-and-excitation networks. In *Proceedings of the IEEE conference on computer vision and pattern recognition*, pp. 7132–7141, 2018.
- Xinyu Huang, Xinjing Cheng, Qichuan Geng, Binbin Cao, Dingfu Zhou, Peng Wang, Yuanqing Lin, and Ruigang Yang. The apolloscape dataset for autonomous driving. In *Proceedings of the IEEE conference on computer vision and pattern recognition workshops*, pp. 954–960, 2018.
- Adrian Kaehler and Gary Bradski. *Learning OpenCV 3: computer vision in C++ with the OpenCV library*. " O'Reilly Media, Inc.", 2016.
- R. Kesten, M. Usman, J. Houston, T. Pandya, K. Nadhamuni, A. Ferreira, M. Yuan, B. Low, A. Jain, P. Ondruska, S. Omari, S. Shah, A. Kulkarni, A. Kazakova, C. Tao, L. Platinsky, W. Jiang, and V. Shet. Level 5 perception dataset 2020. <https://level-5.global/level5/data/>, 2019.
- Harold W Kuhn. The hungarian method for the assignment problem. *Naval research logistics quarterly*, 2(1-2):83–97, 1955.
- Yinhao Li, Zheng Ge, Guanyi Yu, Jinrong Yang, Zengran Wang, Yukang Shi, Jianjian Sun, and Zeming Li. Bevdepth: Acquisition of reliable depth for multi-view 3d object detection. *arXiv preprint arXiv:2206.10092*, 2022.
- Tsung-Yi Lin, Piotr Dollár, Ross Girshick, Kaiming He, Bharath Hariharan, and Serge Belongie. Feature pyramid networks for object detection. In *Proceedings of the IEEE conference on computer vision and pattern recognition*, pp. 2117–2125, 2017.
- Zhijian Liu, Haotian Tang, Alexander Amini, Xingyu Yang, Huizi Mao, Daniela Rus, and Song Han. Bevfusion: Multi-task multi-sensor fusion with unified bird’s-eye view representation. *arXiv*, 2022.

- Jiageng Mao, Minzhe Niu, Chenhan Jiang, Hanxue Liang, Jingheng Chen, Xiaodan Liang, Yamin Li, Chaoqiang Ye, Wei Zhang, Zhenguo Li, et al. One million scenes for autonomous driving: Once dataset. *arXiv preprint arXiv:2106.11037*, 2021.
- Tamás Matuszka and Dániel Kozma. A novel neural network training method for autonomous driving using semi-pseudo-labels and 3d data augmentations. In *Intelligent Information and Database Systems: 14th Asian Conference, ACIIDS 2022, Ho Chi Minh City, Vietnam, November 28–30, 2022, Proceedings, Part II*, pp. 216–229. Springer, 2022.
- Abhishek Patil, Srikanth Malla, Haiming Gang, and Yi-Ting Chen. The h3d dataset for full-surround 3d multi-object detection and tracking in crowded urban scenes. In *2019 International Conference on Robotics and Automation (ICRA)*, pp. 9552–9557. IEEE, 2019.
- Quang-Hieu Pham, Pierre Sevestre, Ramanpreet Singh Pahwa, Huijing Zhan, Chun Ho Pang, Yuda Chen, Armin Mustafa, Vijay Chandrasekhar, and Jie Lin. A* 3d dataset: Towards autonomous driving in challenging environments. In *2020 IEEE International Conference on Robotics and Automation (ICRA)*, pp. 2267–2273. IEEE, 2020.
- Jonah Philion and Sanja Fidler. Lift, splat, shoot: Encoding images from arbitrary camera rigs by implicitly unprojecting to 3d. In *European Conference on Computer Vision*, pp. 194–210. Springer, 2020.
- Rui Qian, Xin Lai, and Xirong Li. 3d object detection for autonomous driving: a survey. *Pattern Recognition*, pp. 108796, 2022.
- Julien Rebut, Arthur Ouaknine, Waqas Malik, and Patrick Pérez. Raw high-definition radar for multi-task learning. In *Proceedings of the IEEE/CVF Conference on Computer Vision and Pattern Recognition*, pp. 17021–17030, 2022.
- Shaoqing Ren, Kaiming He, Ross Girshick, and Jian Sun. Faster r-cnn: Towards real-time object detection with region proposal networks. *Advances in neural information processing systems*, 28, 2015.
- Marcel Sheeny, Emanuele De Pellegrin, Saptarshi Mukherjee, Alireza Ahrabian, Sen Wang, and Andrew Wallace. Radiate: A radar dataset for automotive perception in bad weather. In *2021 IEEE International Conference on Robotics and Automation (ICRA)*, pp. 1–7. IEEE, 2021.
- Richard A Snay and Tomás Soler. Modern terrestrial reference systems (part 1). *Professional Surveyor*, 19(10):32–33, 1999.
- Pei Sun, Henrik Kretschmar, Xerxes Dotiwalla, Aurelien Chouard, Vijaysai Patnaik, Paul Tsui, James Guo, Yin Zhou, Yuning Chai, Benjamin Caine, et al. Scalability in perception for autonomous driving: Waymo open dataset. In *Proceedings of the IEEE/CVF conference on computer vision and pattern recognition*, pp. 2446–2454, 2020.
- Zhi Tian, Chunhua Shen, Hao Chen, and Tong He. Fcos: Fully convolutional one-stage object detection. In *Proceedings of the IEEE/CVF international conference on computer vision*, pp. 9627–9636, 2019.
- Benjamin Wilson, William Qi, Tanmay Agarwal, John Lambert, Jagjeet Singh, Siddhesh Khandelwal, Bowen Pan, Ratnesh Kumar, Andrew Hartnett, Jhony Kaesemodel Pontes, et al. Argoverse 2: Next generation datasets for self-driving perception and forecasting. In *Thirty-fifth Conference on Neural Information Processing Systems Datasets and Benchmarks Track (Round 2)*, 2021.
- Yan Yan, Yuxing Mao, and Bo Li. Second: Sparsely embedded convolutional detection. *Sensors*, 18(10):3337, 2018.
- Tianwei Yin, Xingyi Zhou, and Philipp Krahenbuhl. Center-based 3d object detection and tracking. In *Proceedings of the IEEE/CVF conference on computer vision and pattern recognition*, pp. 11784–11793, 2021.

Yin Zhou and Oncel Tuzel. Voxelnet: End-to-end learning for point cloud based 3d object detection. In *Proceedings of the IEEE conference on computer vision and pattern recognition*, pp. 4490–4499, 2018.

Supplementary Material - aiMotive Dataset: A Multimodal Dataset for Robust Autonomous Driving with Long-Range Perception

1 Dataset documentation (datasheets for datasets)

1.1 Motivation

For what purpose was the dataset created? The reason why the dataset has been created is twofold. First, while several datasets are publicly available, they either do not provide sensor redundancy (i.e. coverage by at least two sensor modalities) which is crucial for robust autonomous driving, or rely only on camera and LiDAR sensors that provide suboptimal performance in adverse weather. Second, the annotation range of these datasets does not exceed 80 meters (with a few exceptions) which is insufficient for training long-range perception systems. The limitation of the annotation range can be explained by the fact that autonomous driving datasets mainly focus on urban environments while ensuring the ability to detect objects in distant regions is critical for highway autonomous driving. Our dataset has an extended annotation range (up to 200 meters) with unique object IDs. Furthermore, it provides a 360-degree FOV using a redundant sensor layout. Due to this solution, the area around the ego vehicle is recorded by at least two different sensors. Therefore, aiMotive dataset can be used for several tasks related to long-range perception (e.g. 3D object detection, end-to-end tracking) and motion prediction.

Who created the dataset (e.g., which team, research group) and on behalf of which entity (e.g., company, institution, organization)? The dataset was created by several internal teams (Vehicle Testing & Engineering, Calibration, aiNotate, Object Detection) on behalf of aiMotive.

Who funded the creation of the dataset? The dataset creation was funded by aiMotive.

1.2 Composition

What do the instances that comprise the dataset represent (e.g., documents, photos, people, countries)? Are there multiple types of instances (e.g., movies, users, and ratings; people and interactions between them; nodes and edges)? The dataset contains multimodal sensor data (camera, radar, LiDAR, GNSS-INS), calibration, and labels. The dataset structure can be seen in Figure 8. Camera sensor data is exported as JPG images for each camera. A LiDAR data file contains a 360-degree revolution of the sensor in compressed las (laz) format. Radar data, GNSS-INS data, calibration, and annotations are stored in JSON files.

How many instances are there in total (of each type, if appropriate)? The dataset includes 26 583 annotated frames with sensor data from multiple modalities. One instance consists of the following:

- Four camera images (front and back cameras with pinhole camera model, left and right cameras with fisheye camera model).
- One LiDAR data item (360-degree revolution).
- Two radar sensor data item as JSON files.
- GNSS-INS data (ego-motion).

```

(000_dir)/
7777777-77777-77-77-77-77(vehicle_name)/
sensor/
  calibration/
    00_session.yml
    aismrotetype_2021_04_01_09_30_47_config.zip
    calibration.json
    extrinsic_matrices.json
  camera/
    (orientation) (type) (position)
    (orientation) (type) (position) 7777777.jpg
    sync_frame200st.json
    gnssins/
      eposition.json
    radar/
      (orientation) (type) (position)
      (orientation) (type) (position) 7777777.json
  dynamic/
    3d_body/
      Frame 7777777.json
    raw_revolutions/
      7777777.laz
  # main folder for all the sequences within an 000
  # sequence ID e.g.: 20210401_093047_09_02_00_00_02_100 Jarvis
  # folder for the exported sensor data in generic format
  # folder for sensor calibration and session description meta files
  # recording configuration of the session
  # sensor configuration for the session
  # calibration parameters for each sensor
  # calibration parameters for each sensor
  # a folder for camera sensor data export
  # a folder for each camera sensor with a specific naming scheme, e.g.: B_MIDRANGECAM_C
  # a camera frame data with sensor identification and frame-ID in jpeg format e.g.: B_MIDRANGECAM_C_0002051.jpg
  # a file containing the received host timestamp for each camera frame-ID
  # a folder for the post-processed GNSS-INS-based trajectory
  # a file containing position and orientation information in ECEF coordinate system for each camera frame's timestamp
  # a folder for the radar sensor export
  # a folder for each radar sensor a specific naming scheme, e.g.: B_LRM_C
  # a radar frame containing radar targets with sensor identification and frame-ID in json format e.g.: B_LRM_C_0002051.json
  # a folder for the dynamic 3d-annotation results
  # a folder for the calculated bounding boxes and metadata of dynamic objects in the session
  # the output folder for the annotation
  # a file containing annotations of dynamic objects at a timestamp. The timestamp is aligned with a camera frame, which is reflected in the name of the file, e.g.: frame_0002051.json
  # LiDAR sensor export (middle position on the top of the car).
  # a Lidar data file containing a 360 degree revolution of the sensor in compressed las (laz) format. Each Lidar point has a 3D position, intensity, and timestamp field.

```

Figure 8: Structure of the dataset.

```

{
  "id": 39831,
  "targets": [
    {
      "azimuth": 0.10969287157958716,
      "elevation": -0.04455072432756424,
      "range": 23.637813568115234,
      "speed": 2.456587314605713,
      "rcs": 26.31393851147461,
      "power": 149.96885681152344,
      "noise": 103.20037078857422
    }
  ]
}

```

Figure 9: A sample of radar data.

- Calibration as JSON files.
- Labels as JSON files.

Does the dataset contain all possible instances or is it a sample (not necessarily random) of instances from a larger set? Yes, the dataset contains all possible instances.

What data does each instance consist of? The camera sensor data corresponding to one instance includes four camera images in JPG format. The back camera resolution is 1920x1216. Other cameras have 1280x704 resolution. A LiDAR data file contains a 360-degree revolution of the sensor in compressed las (laz) format. Each LiDAR point is characterized by its 3D position, intensity, and timestamp. Radar data are stored in JSON files. The sensor measures range, radial speed, azimuth and elevation angle, and reflectivity. These values are provided by the dataset. The speed in raw radar data is the radial speed with a meter/second unit. A radar data sample can be seen in Figure 9. The GNSS-INS data (ego-motion) can be used for transforming relative positions into an absolute coordinate system. The ego-motion-related JSON file contains the following.

- key: camera frame id
- value is a dictionary where:
 - RT_ECEF_body is a matrix from body coordinate system to ECEF
 - enh_sep is the latitude, longitude, height separation, i.e. GNSS error
 - rph_sep is the roll, pitch, heading separation, i.e. IMU error
 - time: GNSS+INS device timestamp
 - time_host: synchronized host timestamp (from camera metadata)

The metadata required for calibrations is stored in a JSON file. A detailed description of the utilized coordinate systems can be found in the paper. The matrices for transforming from sensor to body coordinate system (and vice versa) are stored by the data sensor key (e.g. B_MIDRANGECAM_C). The position of the sensor is stored by 'pos_meter' key defined in the body coordinate system while the orientation of the sensor is described by 'yaw_pitch_roll_deg' key. Camera sensors have additional metadata such as 'focal_length_px', 'principal_point_px', 'image_resolution_px', 'distortion_coeffs', and 'model'.

```

{
  "CapturedObjects": [
    {
      "Absolute Acceleration X": 0.38563060760498847,
      "Absolute Acceleration Y": -1.2683225798807812,
      "Absolute Acceleration Z": 0.0026774359553750992,
      "Absolute Velocity X": 12.694259490966797,
      "Absolute Velocity Y": -0.97118353843688965,
      "Absolute Velocity Z": -0.067227698862552643,
      "ActorName": "CAR_00",
      "BoundingBox3D Extent X": 4.2795677185058594,
      "BoundingBox3D Extent Y": 1.8379080295562744,
      "BoundingBox3D Extent Z": 1.4350985288619995,
      "BoundingBox3D Orientation Quat W": -0.9993588924407959,
      "BoundingBox3D Orientation Quat X": -0.013038261793553829,
      "BoundingBox3D Orientation Quat Y": -0.0021888827844142914,
      "BoundingBox3D Orientation Quat Z": 0.033256486058235168,
      "BoundingBox3D Origin X": 10.013179779852734,
      "BoundingBox3D Origin Y": -3.376384973526001,
      "BoundingBox3D Origin Z": 0.68352939367294312,
      "ObjectId": 0,
      "ObjectType": "CAR",
      "Occluded": 0,
      "Relative Acceleration X": -0.20588822662830353,
      "Relative Acceleration Y": -0.13342832028865814,
      "Relative Acceleration Z": 0.1445978581905365,
      "Relative Velocity X": -0.32385893301963806,
      "Relative Velocity Y": 0.18559594452381134,
      "Relative Velocity Z": -0.0084264581929283142,
      "Truncated": 0
    }
  ],
  "FrameId": 10656,
  "Timestamp": 1762484897000,
  "TimestampMiddle": 1762467897000
}

```

Figure 10: A sample annotation.

Is there a label or target associated with each instance? Yes, each data instance has an associated annotation file. The labels are stored in JSON format where an array stores the annotations of all objects corresponding to the 360-degree surroundings of the ego-vehicle. An example label can be seen in Figure 10.

Is any information missing from individual instances? Occlusion and truncation are currently not calculated for annotated objects. Work is in progress using a PC voxelization-based method. The dataset will be updated when the development is done.

Are relationships between individual instances made explicit (e.g., users’ movie ratings, social network links)? There are no specific relationships between individual instances.

Are there recommended data splits (e.g., training, development/validation, testing)? The dataset is split into 21 402 train and 5 181 validation frames (151/25 train/val scenes). The scenes were recorded in diverse weather and environmental conditions. See Table 3 in the paper for the data distribution. Since the training and validation splits were generated with different methods, some distribution shifts between the data partitions might arise. We investigated the distribution of scenes concerning weather/environment and object count/dimensions and found that training and validation splits are similar in proportion.

Are there any errors, sources of noise, or redundancies in the dataset? The training split has been annotated with an automatic method (see description in paper). The annotated sequences were manually quality-checked based on multiple criteria. The following cases are marked as erroneous in the first phase of the manual quality assurance process:

- Cuboid missing from the object to be annotated (false negative).
 - A phantom box is applied where no object is present to be annotated (false positive).
 - Yaw, pitch, or roll divergence (misaligned box).
 - Misplaced box (position error).
 - More than a 10% divergence between the object size and the cuboid size (size error).
- Multiple cuboids are applied to the same object.

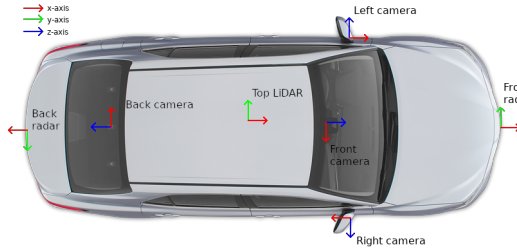


Figure 11: Sensor setup and coordinate systems.

Sensor	Details
1x LiDAR	Spinning, 64 beams, 10Hz capture frequency, 360° horizontal FOV, +15° to -25° vertical FOV, $\leq 200\text{m}$ range, $\pm 2\text{ cm}$ accuracy, up to 1.15 Million Points per Second
2x Radar	18 Hz capture frequency, 77GHz, -16° to +16° azimuth FOV, -7.5 to +7.5 elevation FOV, up to 175m distance, velocity accuracy of $\pm 0.1\text{ m/s}$
4x Camera	2x fisheye: 30 to 60 Hz capture frequency, 1/2.7" CMOS sensor of 1920 \times 1080 resolution, 2x pinhole: 30 to 40 Hz capture frequency, 1/1.55" CMOS sensor of 2896 \times 1876 resolution
1x GNSS+INS	up to 100 Hz measurement frequency, position accuracy of 100 mm (PPK), heading accuracy of 0.044°, roll&pitch accuracy of 0.009°

Table 9: Description of used sensors.

During this inspection, the amodal bounding boxes are projected back to all available cameras. The oriented bounding boxes are inspected from the top view too. The manual quality checking is performed on the scene level. When a scene has been validated by one of the manual laborers, it goes through a second phase where the manual quality-checking supervisor can either confirm it or send it back for recheck. In the case of a recheck, phase one has to be performed again.

Some label noise still might be in the dataset even though we aimed to minimize it via human validation. In this way, we selected sufficiently accurately labeled recordings, and most scenes with erroneous annotations were discarded.

Is the dataset self-contained, or does it link to or otherwise rely on external resources (e.g., websites, tweets, other datasets)? The dataset is self-contained and available on GitHub and Kaggle.

Does the dataset contain data that might be considered confidential (e.g., data that is protected by legal privilege or by doctor-patient confidentiality, data that includes the content of individuals' non-public communications)? No, the dataset does not contain confidential data.

Does the dataset contain data that, if viewed directly, might be offensive, insulting, threatening, or might otherwise cause anxiety? To the best of our knowledge, it does not contain offensive content.

1.3 Collection process

How was the data associated with each instance acquired? The data associated with each instance is directly observable and exported from the raw sensor data (e.g. camera, radar, LiDAR).

What mechanisms or procedures were used to collect the data (e.g., hardware apparatuses or sensors, manual human curation, software programs, software APIs)? The data was recorded using a roof-mounted, rotating 64-beam LiDAR, four cameras, and two long-range radars, providing 360° coverage with sensor redundancy. The localization was based on a high-precision GNSS+INS sensor. Additional details can be found in Figure 11 and Table 9. The data was collected in three countries on two continents with four cars to provide a diverse dataset. The recordings have taken place in California, US; Austria; and Hungary using three Toyota Camry and one Toyota Prius. The validity of sensor data was manually checked using aiMotive Dataset Loader.

If the dataset is a sample from a larger set, what was the sampling strategy (e.g., deterministic, probabilistic with specific sampling probabilities)? The dataset has not been sampled from a larger set.

Who was involved in the data collection process (e.g., students, crowdworkers, contractors) and how were they compensated (e.g., how much were crowdworkers paid)? The data collection process was performed by full-time aiMotive employees. The process did not involve students, crowdworkers, or contractors. The data collection process was part of the employee responsibilities of the participants, who were compensated by monthly salaries.

Over what timeframe was the data collected? Does this timeframe match the creation timeframe of the data associated with the instances (e.g., recent crawl of old news articles)? The recording phase of the footage was spread across a year to gather data on different seasons and weather conditions. The annotation creation did not depend on the time of raw sensor data recording.

Were any ethical review processes conducted (e.g., by an institutional review board)? The data collection method has satisfied the requirements given by the Institutional Review Board. The details can be read in aiMotive’s Data Protection Policy.

1.4 Preprocessing/cleaning/labeling

Was any preprocessing/cleaning/labeling of the data done (e.g., discretization or bucketing, tokenization, part-of-speech tagging, SIFT feature extraction, removal of instances, processing of missing values)? The dataset has been anonymized by blurring faces and license plates. Besides this preprocessing step, no additional method has been applied to raw sensor data.

Was the “raw” data saved in addition to the preprocessed/cleaned/labeled data (e.g., to support unanticipated future uses)? If so, please provide a link or other access point to the “raw” data. No, the raw data has not been saved to meet GDPR requirements.

Is the software that was used to preprocess/clean/label the data available? Yes, Dash-camCleaner (face and license plate blurring software) is available on GitHub.

1.5 Uses

Has the dataset been used for any tasks already? The dataset has been downloaded 100+ times by other researchers and students at the time of submission. Statistics can be found on Kaggle.

Is there a repository that links to any or all papers or systems that use the dataset? Yes, the dataset can be found on Papers With Code.

What (other) tasks could the dataset be used for? The dataset can be used for end-to-end long-range multiple object tracking, motion prediction, visual and LiDAR odometry, and contrastive self-supervised representation learning.

Is there anything about the composition of the dataset or the way it was collected and preprocessed/cleaned/labeled that might impact future uses? To the best of our knowledge, there is no such case.

Are there tasks for which the dataset should not be used? The dataset must not be used for any military or harmful application.

1.6 Distribution

Will the dataset be distributed to third parties outside of the entity (e.g., company, institution, organization) on behalf of which the dataset was created? The dataset has been uploaded to Kaggle. In this way, researchers with limited computational capacities can utilize the Kaggle platform for training models on the dataset.

How will the dataset will be distributed (e.g., tarball on website, API, GitHub)? Does the dataset have a digital object identifier (DOI)? The dataset is available on GitHub and Kaggle. The digital object identifier (DOI) is 10.34740/kaggle/ds/2738461.

When will the dataset be distributed? The dataset is already available.

Will the dataset be distributed under a copyright or other intellectual property (IP) license, and/or under applicable terms of use (ToU)? The dataset is available under Creative Commons' Attribution-NonCommercial-ShareAlike 4.0 International (CC BY-NC-SA 4.0) licence.

Have any third parties imposed IP-based or other restrictions on the data associated with the instances? No.

Do any export controls or other regulatory restrictions apply to the dataset or to individual instances? No.

1.7 Maintenance

Who will be supporting/hosting/maintaining the dataset? The dataset is supported, hosted, and maintained by aiMotive.

How can the owner/curator/manager of the dataset be contacted (e.g., email address)? The dataset owner can be contacted at tamas.matuszka@aimotive.com.

Is there an erratum? Currently, there is no erratum.

Will the dataset be updated (e.g., to correct labeling errors, add new instances, delete instances)? The dataset will be updated to correct labeling errors in case of found errors. New instance addition might also happen. The updates will be disseminated on GitHub and Kaggle.

If the dataset relates to people, are there applicable limits on the retention of the data associated with the instances (e.g., were the individuals in question told that their data would be retained for a fixed period of time and then deleted)? To the best of our knowledge, there is no such limit.

Will older versions of the dataset continue to be supported/hosted/maintained? The dataset will continuously be supported/maintained on GitHub.

If others want to extend/augment/build on/contribute to the dataset, is there a mechanism for them to do so? Contributions are welcome. Pull requests can be sent to our GitHub repositories. In order to be merged into the main branch, at least one review and approval from the code owners are needed. In this way, the contribution can be validated. In terms of dataset augmentation/extension, please contact the dataset owner. One of the main goals of the release of the dataset is to facilitate research in multimodal sensor fusion and robust long-range perception systems. Therefore, building on our dataset is encouraged.

A Appendix

A.1 Samples and qualitative results

In this section, we provide qualitative results and several visual examples of the annotations contained by the dataset. Figure 12 (VRU annotation) and 13 (tunnel, heavy rain, dense urban environment) show example annotations generated by our automatic annotation method and manual annotation, respectively. A short video about the camera projection of the annotations created by the automatic annotation method can be seen in this link. Figure 14 visualizes a sample detection of the LiDAR+radar baseline model on the validation set. Note that this sample is not included in the training set. It is the output of one of the baseline models described in the paper.

Figure 15 and 16 visualize how well the bounding boxes fit individual sensor modalities (sensor and bounding box visualization from top to down: LiDAR, radar, camera: back and front). The sensor setup can result in a synchronization limitation caused by the fact that sensors differ in the temporal recording method. Since the rotating LiDAR and rolling shutter cameras have different measurement methods, there are some discrepancies in temporally discretized annotations. This phenomenon is mostly visible when the relative speed difference between the ego and exo car is large. As the figures show, the radar sensor has a visible variance (see distant objects in front of the ego car). The bounding boxes in the distant area might be slightly shifted from the LiDAR point cloud too, as can be seen in the case of the last vehicle behind the ego car in Figure 15 (best viewed by zooming in).



Figure 12: Example motorbike GT created by automatic annotation.



Figure 13: Example ground truth annotations from the training set.

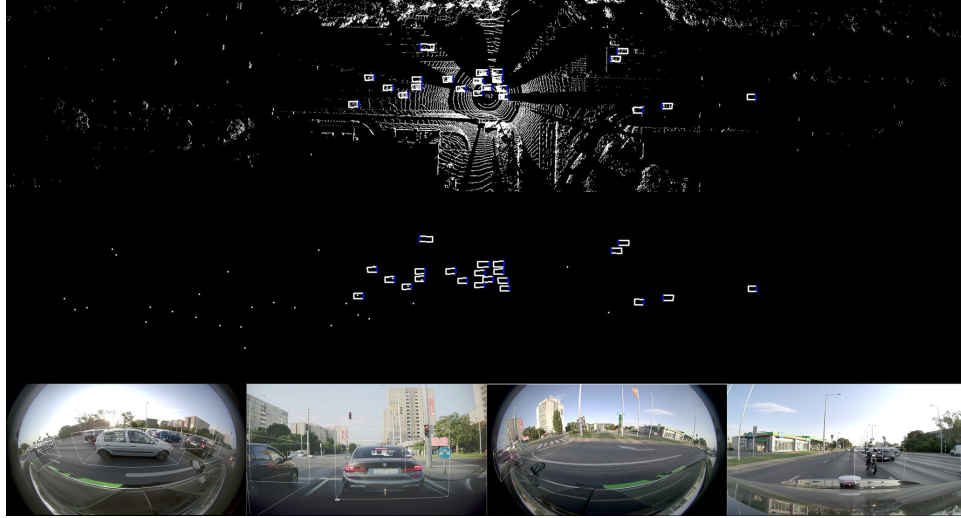


Figure 14: Qualitative results: detections of the LiDAR+radar baseline model on validation set. Top row: detections on LiDAR point cloud. Middle row: detections on radar targets, bottom row (from left to right): detections on left, front, right, and back cameras.



Figure 15: Bounding boxes fitting to individual sensors (best viewed by zooming in) - distant annotations.



Figure 16: Bounding boxes fitting to individual sensors (best viewed by zooming in) - dense annotations.

A.2 Additional evaluation results

In this section, we provide additional evaluations of the trained baseline models using the AP-R40, classification accuracy, and Average Orientation Similarity (AOS) metrics. The models were trained for 9 epochs. Furthermore, to investigate the effect of distance on the detection ability, we evaluated our models on various depth ranges (distance range is measured from the ego vehicle, both behind and in front of it).

Modalities	Highway	Urban	Night	Rain	Full	Class. Acc.	AOS
LiDAR	0.753	0.619	0.752	0.551	0.654	0.840	0.731
LiDAR, camera	0.746	0.631	0.767	0.442	0.656	0.839	0.748
LiDAR, radar	0.743	0.632	0.768	0.496	0.654	0.836	0.904
LiDAR, radar, camera	0.719	0.618	0.736	0.421	0.649	0.839	0.889

Table 10: Comparison of baseline models using AP-R40 (on splits and over the full dataset), classification accuracy, and AOS metrics averaged over val set.

Modalities	Highway	Urban	Night	Rain	Full	Class. Acc.	AOS
LiDAR	0.497	0.446	0.437	0.587	0.459	0.756	0.858
LiDAR, camera	0.494	0.452	0.499	0.495	0.462	0.751	0.793
LiDAR, radar	0.477	0.490	0.512	0.630	0.495	0.749	0.869
LiDAR, radar, camera	0.461	0.461	0.474	0.410	0.464	0.734	0.876

Table 11: Comparison of baseline models in the distant region (>75m) using AP-R40 (on splits and over the full dataset), classification accuracy, and AOS metrics averaged over val set.

A.2.1 Range-based evaluation: [0-30) m

Modalities	Highway	Urban	Night	Rain
LiDAR	0.937	0.617	0.844	0.313
LiDAR, camera	0.911	0.652	0.847	0.292
LiDAR, radar	0.932	0.631	0.824	0.195
LiDAR, radar, camera	0.906	0.621	0.802	0.233

Table 12: Comparison of baseline models in the range of [0-30) m from ego car using all points interpolation AP metric.

Modalities	Highway	Urban	Night	Rain
LiDAR	0.894	0.605	0.823	0.325
LiDAR, camera	0.876	0.620	0.828	0.325
LiDAR, radar	0.890	0.615	0.773	0.236
LiDAR, radar, camera	0.877	0.608	0.772	0.273

Table 13: Comparison of baseline models in the range of [0-30) m from ego car using 11-points AP metric.

Modalities	Highway	Urban	Night	Rain
LiDAR	0.925	0.606	0.829	0.302
LiDAR, camera	0.901	0.639	0.833	0.284
LiDAR, radar	0.921	0.616	0.809	0.187
LiDAR, radar, camera	0.891	0.610	0.791	0.225

Table 14: Comparison of baseline models in the range of [0-30) m from ego car using AP-R40 metric.

Modalities	AP-all	AP-11	AP-R40	Class. Acc.	AOS
LiDAR	0.671	0.665	0.654	0.863	0.937
LiDAR, camera	0.691	0.681	0.677	0.863	0.866
LiDAR, radar	0.674	0.669	0.659	0.858	0.913
LiDAR, radar, camera	0.664	0.662	0.652	0.871	0.867

Table 15: Comparison of baseline models in the range of [0-30) m from ego car on the whole dataset using all points, 11-points AP, and AP-R40, classification accuracy, and AOS metrics.

A.2.2 Range-based evaluation: [30-60] m

Modalities	Highway	Urban	Night	Rain
LiDAR	0.933	0.672	0.766	0.772
LiDAR, camera	0.922	0.676	0.796	0.632
LiDAR, radar	0.924	0.664	0.790	0.686
LiDAR, radar, camera	0.924	0.670	0.786	0.645

Table 16: Comparison of baseline models in the range of [30-60] m from ego car using all points interpolation AP metric.

Modalities	Highway	Urban	Night	Rain
LiDAR	0.888	0.664	0.739	0.751
LiDAR, camera	0.879	0.668	0.769	0.621
LiDAR, radar	0.886	0.625	0.760	0.680
LiDAR, radar, camera	0.883	0.663	0.769	0.623

Table 17: Comparison of baseline models in the range of [30-60] m from ego car using 11-points AP metric.

Modalities	Highway	Urban	Night	Rain
LiDAR	0.920	0.661	0.754	0.761
LiDAR, camera	0.910	0.662	0.784	0.621
LiDAR, radar	0.913	0.649	0.777	0.675
LiDAR, radar, camera	0.914	0.662	0.776	0.633

Table 18: Comparison of baseline models in the range of [30-60] m from ego car using AP-R40 metric.

Modalities	AP-all	AP-11	AP-R40	Class. Acc.	AOS
LiDAR	0.722	0.697	0.706	0.873	0.944
LiDAR, camera	0.723	0.695	0.712	0.873	0.892
LiDAR, radar	0.716	0.696	0.704	0.873	0.924
LiDAR, radar, camera	0.722	0.702	0.711	0.873	0.931

Table 19: Comparison of baseline models in the range of [30-60] m from ego car on the whole dataset using all points, 11-points AP, and AP-R40, classification accuracy, and AOS metrics.

A.2.3 Range-based evaluation: (60-120] m

Modalities	Highway	Urban	Night	Rain
LiDAR	0.773	0.612	0.667	0.755
LiDAR, camera	0.796	0.615	0.690	0.700
LiDAR, radar	0.776	0.629	0.703	0.739
LiDAR, radar, camera	0.813	0.637	0.669	0.594

Table 20: Comparison of baseline models in the range of [60-120) m from ego car using all points interpolation AP metric.

Modalities	Highway	Urban	Night	Rain
LiDAR	0.739	0.586	0.656	0.727
LiDAR, camera	0.772	0.599	0.680	0.684
LiDAR, radar	0.740	0.613	0.694	0.723
LiDAR, radar, camera	0.796	0.613	0.646	0.575

Table 21: Comparison of baseline models in the range of [60-120) m from ego car using 11-points AP metric.

Modalities	Highway	Urban	Night	Rain
LiDAR	0.761	0.596	0.657	0.743
LiDAR, camera	0.786	0.599	0.678	0.690
LiDAR, radar	0.764	0.615	0.692	0.730
LiDAR, radar, camera	0.804	0.625	0.654	0.578

Table 22: Comparison of baseline models in the range of [60-120) m from ego car using AP-R40 metric.

Modalities	AP-all	AP-11	AP-R40	Class. Acc.	AOS
LiDAR	0.639	0.637	0.624	0.798	0.834
LiDAR, camera	0.631	0.629	0.618	0.798	0.803
LiDAR, radar	0.659	0.628	0.642	0.793	0.871
LiDAR, radar, camera	0.668	0.665	0.656	0.790	0.874

Table 23: Comparison of baseline models in the range of [60-120) m from ego car on the whole dataset using all points, 11-points AP, and AP-R40, classification accuracy, and AOS metrics.

A.2.4 Range-based evaluation: [120-200] m

Modalities	Highway	Urban	Night	Rain
LiDAR	0.307	0.194	0.132	0.316
LiDAR, camera	0.295	0.184	0.183	0.154
LiDAR, radar	0.289	0.272	0.253	0.402
LiDAR, radar, camera	0.205	0.157	0.277	0.155

Table 24: Comparison of baseline models in the range of [120-200] m from ego car using all points interpolation AP metric.

Modalities	Highway	Urban	Night	Rain
LiDAR	0.341	0.217	0.133	0.334
LiDAR, camera	0.316	0.220	0.203	0.199
LiDAR, radar	0.310	0.260	0.270	0.395
LiDAR, radar, camera	0.239	0.186	0.292	0.167

Table 25: Comparison of baseline models in the range of [120-200] m from ego car using 11-points AP metric.

Modalities	Highway	Urban	Night	Rain
LiDAR	0.301	0.187	0.128	0.302
LiDAR, camera	0.286	0.170	0.176	0.144
LiDAR, radar	0.280	0.262	0.242	0.389
LiDAR, radar, camera	0.187	0.148	0.265	0.149

Table 26: Comparison of baseline models in the range of [120-200] m from ego car using AP-R40 metric.

Modalities	AP-all	AP-11	AP-R40	Class. Acc.	AOS
LiDAR	0.249	0.272	0.237	0.750	0.883
LiDAR, camera	0.235	0.264	0.224	0.726	0.784
LiDAR, radar	0.279	0.296	0.271	0.729	0.901
LiDAR, radar, camera	0.187	0.222	0.178	0.673	0.884

Table 27: Comparison of baseline models in the range of [120-200] m from ego car on the whole dataset using all points, 11-points AP, and AP-R40, classification accuracy, and AOS metrics.

A.2.5 Camera-only baseline model

The camera-only baseline model is adapted from BEVDepth repository⁴. We changed the image backbone from ResNet-50 to ResNet-152 to utilize a stronger image encoder. This baseline model performed very poorly (<0.10 AP-R40) on the whole perception range (± 200 meters in longitudinal, ± 25.6 meters in lateral direction). We investigated the heatmap tensors and found that the model is very uncertain in distant regions. This fact results in a large number of false positive detections. This might explain the unexpected multimodal results in some cases since this phenomenon might hinder the multimodal feature fusion. The AP-R40 performance in the near-region (<30 m) is also worse than our other unimodal baseline model, though (camera-only: 0.406, LiDAR-only: 0.677).

Nevertheless, the combination of the camera-only model with additional sensor modalities resulted in better performance on the urban/night splits and the whole dataset (on the entire perception range) using the AP-R40 metrics (Table 10). The improvement is even

⁴<https://github.com/Megvii-BaseDetection/BEVDepth>

more visible in distant regions (Table 11, Table 20-23). Finally, we would like to solicit contributions from the research community in order to develop more performant unimodal and multimodal models.